Theory for a dissipative droplet soliton excited by a spin torque nanocontact

M. A. Hoefer,[1,*] T. J. Silva,[2] and Mark W. Keller[2]

[1]*Department of Mathematics, North Carolina State University, Raleigh, North Carolina 27695, USA*

[2]*National Institute of Standards and Technology, Boulder, Colorado 80305, USA*

A distinct type of solitary wave is predicted to form in spin torque oscillators when the free layer has a sufficiently large perpendicular anisotropy. In this structure, which is a dissipative version of the conservative droplet soliton originally studied in 1977 by Ivanov and Kosevich, spin torque counteracts the damping that would otherwise destroy the mode. Asymptotic methods are used to derive conditions on perpendicular anisotropy strength and applied current under which a dissipative droplet can be nucleated and sustained. Numerical methods are used to confirm the stability of the droplet against various perturbations that are likely in experiments, including tilting of the applied field, nonzero spin torque asymmetry, and nontrivial Oersted fields. Under certain conditions, the droplet experiences a drift instability in which it propagates away from the nanocontact and is then destroyed by damping.

I. INTRODUCTION

The concept of a soliton as a localized particlelike excitation that preserves its shape can be extended to systems that are far from thermodynamic equilibrium through the concept of a "dissipative soliton."[1] This enables the analysis of a broad range of physical, chemical, and biological nonlinear systems in which localized excitations are observed. Driven magnetic systems, especially those of technological interest, exhibit strongly nonlinear dynamics and are an ideal experimental domain for exploring the dissipative soliton model.

In this paper, we provide an analytical theory for a novel, localized oscillation mode in a spin torque oscillator with a free layer having perpendicular magnetic anisotropy. The salient features of this mode include a frequency well below that of uniform ferromagnetic resonance, a weak dependence of frequency on bias current and a precession angle at the maximal value of 90°. Combining numerical micromagnetic simulations with an asymptotic analysis of the equations of motion, we identify this mode as a dynamic, dissipative magnetic soliton that is closely related to the "magnon droplet" predicted by Ivanov and Kosevich in 1977.[2,3] The mode central region exhibits magnetization pointing nearly opposite to its equilibrium direction with a perimeter manifesting 90° precession. From our asymptotic analysis, we derive conditions on perpendicular anisotropy and bias current for the nucleation and existence of the dissipative droplet. Using our numerical simulations, we analyze the stability of the dissipative droplet soliton as a function of applied magnetic field, bias current, and spin torque asymmetry.

Solitons in conservative systems occur when nonlinear terms in the equation of motion balance the effects of dispersion.[4] A classic example is a light pulse moving in a lossless optical fiber: the change of refractive index with frequency (dispersion) tends to make the pulse spread out, but for a certain pulse shape, the change in refractive index with light intensity due to the optical Kerr effect (nonlinearity) exactly balances the dispersion. Pulses having this shape can propagate without spreading and are called solitary waves or

solitons. The balance between nonlinearity and dispersion typically allows for the existence of a continuous family of solitons that can be excited in the system, rather than a single solution. In the optical fiber example, the family can be parametrized, for example, by pulse amplitude, and there is a continuous range of amplitudes that satisfy the soliton balancing condition.

Dissipative solitons[1] are characterized by an additional balancing condition between gain and loss that typically allows for only a single solution for a given set of parameters. Although conservative soliton models can explain weakly nonlinear behavior seen in magnetic systems of exceptionally low damping,[5] damping is not a small effect for many magnetic systems of both fundamental and technological interest. By combining classical soliton theory with bifurcation theory of nonlinear dynamics and concepts of self-organization the dissipative soliton concept provides a framework for describing a broad range of solitonlike behaviors. Here, we apply this concept to a nanoscale ferromagnetic system in which both damping and a driving force (spin torque) are important.

Spin torque[6–8] occurs when a current is driven through a structure with alternating magnetic and nonmagnetic layers in which spin-dependent conductance at the interfaces results in a spin-polarized electron flow. When the polarized electrons enter a ferromagnetic layer whose magnetization **M** is not collinear with the electron spins, the transmitted spins are rotated toward **M** and the angular momentum absorbed by the ferromagnetic layer is known as the spin torque. Typical devices have two ferromagnetic layers through which current is driven: a thick "fixed" layer that determines the direction of electron polarization, and a thin "free" layer whose orientation can be readily changed by spin torque. For current of the appropriate polarity, spin torque opposes the intrinsic damping torque in the system, and currents above a threshold produce dynamic states in which **M** of the free layer can be manipulated without applying a magnetic field. This effect has been used to control switching of nanoscale magnetic elements[9] with potential applications in computer memory and data storage. The effect has also been used to produce coherent, frequency-tunable microwave oscillations[10] in a
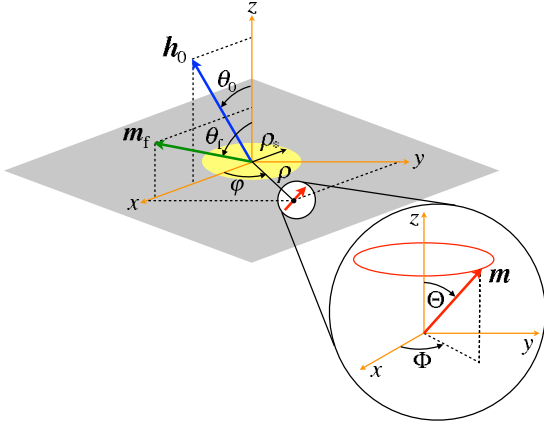
FIG. 1. (Color online) Schematic of nanocontact (yellow central disk of radius ρ_*), the domain of **m** ($\mathbb{R}^2$ in polar coordinates with radius ρ, azimuthal angle φ), the range of **m** (unit sphere $\mathbb{S}^2$ with polar angle Θ, azimuthal angle Φ), orientations of the applied field $\mathbf{h}_0$ and fixed layer $\mathbf{m}_f$.

nanoscale device known as a spin torque oscillator (STO) with potential applications in integrated microwave circuits for mixing and active phase control. Recent reviews cover the physics of spin torque[11] and its possible applications.[12]

The equations of motion for **M** in the presence of spin torque (presented below) are inherently nonlinear and their full solution for a general case is often studied by use of numerical methods. Analytical methods can sometimes be applied by invoking restrictions such as high-symmetry, spatially uniform **M** (the "macrospin" model), and small precession amplitude (small angle between **M** and its equilibrium direction). These restricted cases have been used to explain experimental results with mixed success. The local nature of spin torque allows it to drive large amplitude excitations in which **M** varies on the scale of the magnetic exchange length (typically a few nanometers), something that applied magnetic fields cannot do. As we show here, this regime of strongly nonlinear, strongly nonuniform, sustained magnetodynamics is amenable to theoretical examination using numerical and analytical approaches. This regime is also experimentally accessible in STOs.

We note that a different type of magnetic soliton generated by spin torque, called a spin wave "bullet," was predicted by Slavin and Tiberkevich in 2005 to occur in the point-contact geometry with magnetic films exhibiting in-plane oriented anisotropy and in-plane applied magnetic field.[13] For this case, the precession frequency decreases with increasing current, which can result in localization if the frequency falls below the bottom of the spin wave band at the ferromagnetic resonance (FMR) frequency. The weakly nonlinear bullet soliton is a solution to a Nonlinear Schrödinger-type equation with third-order nonlinearity in the excitation amplitude. As such, its predicted experimental signature consists of subtle shifts in microwave output frequency and threshold current relative to that expected for a nonlocalized mode. In contrast, the droplet soliton studied here exhibits dramatic differences in behavior from that of a nonlocalized mode. This is due to the fact that it is a strongly nonlinear solution of the full equations of motion rather than simply a third order expansion.

Domain walls,[14] magnetic bubbles,[15] and vortices[16] are examples of well-studied, strongly nonlinear, localized structures that occur in magnetic materials. The droplet differs from these static structures in that it is inherently dynamic; the frequency of spin precession within the droplet is always greater than zero. In this work, we focus on the two-dimensional (2D), nontopological droplet, but we note that droplets in two and three dimensions come in topological flavors as well.[3]

We begin in the next section by presenting an asymptotic analysis of the model equations for the dissipative droplet in a high-symmetry case. We will also derive the droplet's frequency vs current relation in this section. Section III is devoted to the study of droplets in physically realistic situations incorporating the current-induced Oersted field as well as canting of the applied field and fixed layer. Section IV details experimentally accessible nucleation conditions for a droplet that take advantage of a small amplitude instability. In Sec. V, we discuss possible extensions of the theory and we relate the droplet to other excitations in thin magnetic films. We conclude in Sec. VI with a summary of the droplet's unique properties. Appendices A and B provide details of our stability calculation and numerical method, respectively.

II. DROPLET IN A NANOCONTACT

We consider the Landau-Lifshitz-Slonczewski equation in nondimensional form[6,11] describing the free layer magnetization in polar coordinates [$\mathbf{m} = \mathbf{m}(\rho, \varphi, t)$; bold symbols represent vectors in $\mathbb{R}^3$ or $\mathbb{R}^2$, contextually dependent; e.g., $\mathbf{m} = [m_x, m_y, m_z]$]

$$\frac{\partial \mathbf{m}}{\partial t} = \underbrace{-\mathbf{m} \times \mathbf{h}_{\text{eff}}}_{\text{precession}} \underbrace{- \alpha \mathbf{m} \times (\mathbf{m} \times \mathbf{h}_{\text{eff}})}_{\text{damping}}$$
$$+ \underbrace{\frac{\sigma V(\rho)}{1 + \nu \mathbf{m} \cdot \mathbf{m}_f} \mathbf{m} \times (\mathbf{m} \times \mathbf{m}_f)}_{\text{spin torque}}, \quad \mathbf{m} : \mathbb{R}^2 \to \mathbb{S}^2,$$

$$\mathbf{h}_{\text{eff}} = \nabla^2 \mathbf{m} + \mathbf{h}_0 + \mathbf{h}_{\text{oe}} + (h_k - 1) m_z \mathbf{z}, \quad |\mathbf{m}| \equiv 1. \quad (1)$$

Figure 1 is a schematic of the nanocontact geometry and coordinate systems considered in this work. The magnetization $\mathbf{m} = \mathbf{M}/M_s$ and fields (e.g., $\mathbf{h}_0 = \mathbf{H}_0/M_s$) are normalized by the saturation magnetization M_s, time is normalized by $2\pi/|\gamma|\mu_0 M_s$ (γ is the gyromagnetic ratio and μ_0 is the permeability of free space), and space is normalized by the exchange length $l_{\text{ex}} = \sqrt{D/|\gamma|\mu_0 M_s \hbar}$ (D is the exchange parameter and $\hbar$ is the reduced Planck's constant). We consider a free layer whose thickness δ is much smaller than the magnetic excitation wavelengths so that a 2D model with local dipolar fields is justified.[17] The precessional term is driven by the effective field $\mathbf{h}_{\text{eff}}$ incorporating exchange $\nabla^2 \mathbf{m}$, a uniform applied field $\mathbf{h}_0 = h_0[\sin \theta_0, 0, \cos \theta_0]$ ($h_0 \geq 0$), the current-induced Oersted field $\mathbf{h}_{\text{oe}} = -f_{\text{oe}}(\rho)\boldsymbol{\varphi}$ (the definition of f_{oe} is given in Ref. 18 and summarized in Sec. III A), the perpendicular field $h_k m_z \mathbf{z}$ due to crystal anisotropy ($h_k > 1$), and the demagnetizing field for a thin film $-m_z \mathbf{z}$. The Landau-Lifshitz damping coefficient is α. The spin torque
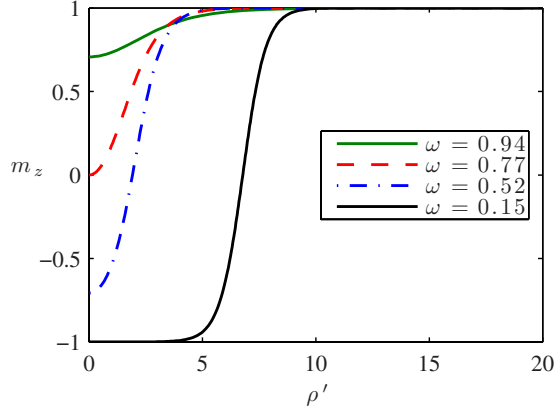
FIG. 2. (Color online) Conservative droplet profiles with $m_z = \cos \Theta_0$.

term involves $\sigma = I/I_c$, where I is the current, $I_c = (\lambda^2 + 1)2M_s^2 e \mu_0 \pi r_*^2 \delta/(\hbar P \lambda^2)$ (P and $\lambda \geq 1$ are the polarization and spin torque asymmetry parameters, respectively,[6] e is the electron charge, r_* is the nanocontact radius), $\nu = (\lambda^2 - 1)/(\lambda^2 + 1)$ ($0 \leq \nu < 1$), and $V(\rho) = \mathcal{H}(\rho_* - \rho)$, where $\mathcal{H}$ is the Heaviside step function, $\rho_* = r_*/l_{ex}$ is the nondimensional contact radius, and $\mathbf{m}_f = [\sin \theta_f, 0, \cos \theta_f]$ is the uniform fixed layer magnetization.

Numerical computations of Eq. (1) will be presented in Sec. III by means of a method discussed in Appendix B. For the rest of this section, we will focus on a high-symmetry case where

$$\text{high symmetry case:} \quad \theta_0 = 0, \quad \mathbf{h}_{oe} \equiv 0. \quad (2)$$

For the analysis of this case, it is helpful to consider Eq. (1) in spherical coordinates

$$\mathbf{m} = [\cos \Phi \sin \Theta, \sin \Phi \sin \Theta, \cos \Theta]$$

(see Fig. 1)

$$\frac{\partial \Theta}{\partial t} = F[\Theta, \Phi] - \alpha G[\Theta, \Phi] + \sigma V(\rho) P_\Theta[\Theta, \Phi], \quad (3)$$

$$\sin \Theta \frac{\partial \Phi}{\partial t} = G[\Theta, \Phi] + \alpha F[\Theta, \Phi] + \sigma V(\rho) P_\Phi[\Theta, \Phi], \quad (4)$$

where

$$F[\Theta, \Phi] = \sin \Theta \nabla^2 \Phi + 2 \cos \Theta \, \nabla \Phi \cdot \nabla \Theta,$$

$$G[\Theta, \Phi] = -\nabla^2 \Theta + \frac{1}{2} \sin 2\Theta (|\nabla \Phi|^2 + h_k - 1) + h_0 \sin \Theta,$$

$$P_\Theta[\Theta, \Phi] = \frac{-\cos \Theta \cos \Phi \sin \theta_f + \sin \Theta \cos \theta_f}{1 + \nu(\cos \Phi \sin \Theta \sin \theta_f + \cos \Theta \cos \theta_f)},$$

$$P_\Phi[\Theta, \Phi] = \frac{\sin \Phi \sin \theta_f}{1 + \nu(\cos \Phi \sin \Theta \sin \theta_f + \cos \Theta \cos \theta_f)}.$$

The polar angle Θ satisfies $0 \leq \Theta \leq \pi$ while the azimuthal angle Φ is interpreted modulo 2π.

In the symmetric case of Eq. (2), we can remove the explicit dependence on h_k from Eqs. (3) and (4) by introducing the following rescaling:

$$\rho = \rho'/\sqrt{h_k - 1}, \quad t = t'/(h_k - 1),$$

$$\sigma = (h_k - 1)\sigma', \quad h_0 = (h_k - 1)h_0', \quad \rho_* = \rho_*/\sqrt{h_k - 1}. \quad (5)$$

Recall that we are assuming $h_k > 1$. Then, with the scalings in Eq. (5) and dividing Eqs. (3) and (4) by $h_k - 1$, we can, without loss of generality, take $h_k - 1 = 1$. For the rest of this Sec. II, we will use the scalings in Eq. (5) so that $h_k \to 2$.

In this section, we consider localized magnetization configurations that satisfy

$$\lim_{\rho' \to \infty} \Theta(\rho', \varphi, t') = 0$$

with sufficiently rapid decay. As such, we define the magnetic energy in terms of exchange and anisotropy energy via

$$\mathcal{E}[\Theta, \Phi] = \frac{1}{2} \int_{\mathbb{R}^2} [\underbrace{|\nabla \Theta|^2 + \sin^2 \Theta |\nabla \Phi|^2}_{\text{exchange}} + \underbrace{\sin^2 \Theta}_{\text{anisotropy}}] d\mathbf{r}'.$$

Note that the damping and spin torque terms break energy conservation

$$\frac{d\mathcal{E}}{dt}[\Theta, \Phi] = \int_{\mathbb{R}^2} \{\sigma'[(G[\Theta, \Phi] - h_0' \sin \Theta)P_\Theta[\Theta, \Phi]$$

$$- F[\Theta, \Phi]P_\Phi[\Theta, \Phi]] - \alpha[(G[\Theta, \Phi] - h_0' \sin \Theta)^2$$

$$+ F[\Theta, \Phi]^2]\} d\mathbf{r}'. \quad (6)$$

A. Conservative droplet soliton

In the absence of damping and spin torque ($\alpha = 0$, $\sigma' = 0$), Eqs. (3) and (4) admit a continuous family of exponentially localized, nontopological solutions known as magnon droplet solitons.[2,3] These solutions can be parametrized by the frequency ω_0 and written as

$$\Theta \equiv \Theta_0(\rho; \omega_0),$$

$$\Phi \equiv (\omega_0 + h_0')t', = [\omega_0(h_k - 1) + h_0]t. \quad (7)$$

They satisfy a balance between exchange (dispersion) and anisotropy (nonlinearity) through the nonlinear eigenvalue problem

$$F[\Theta_0, (\omega_0 + h_0')t'] = 0,$$

$$G[\Theta_0, (\omega_0 + h_0')t'] = (\omega_0 + h_0')\sin \Theta_0,$$

or

$$\left(\frac{d^2}{d\rho'^2} + \frac{1}{\rho'}\frac{d}{d\rho'}\right)\Theta_0 - \frac{1}{2}\sin 2\Theta_0 + \omega_0 \sin \Theta_0 = 0 \quad (8)$$

with the boundary conditions

$$\frac{d\Theta_0}{d\rho'}(0; \omega_0) = 0, \quad \lim_{\rho' \to \infty} \Theta_0(\rho'; \omega_0) = 0. \quad (9)$$

The conservative droplet solutions in Eqs. (7)–(9) have the following properties. The polar angle Θ_0 varies with radial distance and is independent of time; thus the spatial distribution of $m_z = \cos \Theta_0$ is static and azimuthally symmetric. The azimuthal angle Φ is independent of position and varies linearly in time; thus all points precess at a common frequency and in phase. It has been shown that[2,3] ω_0 satisfies

$$0 < \omega_0 < 1. \tag{10}$$

Therefore, the total precessional frequency $\omega_0 + h_0'$ varies between the Zeeman frequency h_0' and the frequency of spatially uniform precession about $\Theta = 0$, $1 + h_0'$ (the FMR frequency).

While the conservative droplet does not have a closed-form analytical expression, we calculate it by numerically solving Eq. (8) subject to the boundary conditions in Eq. (9) with the function BVP4C in Matlab®. A plot of several conservative droplet profiles is shown in Fig. 2. We see that the amplitude at the origin $1 - m_z(0; \omega_0) = 1 - \cos \Theta_0(0; \omega_0)$ decreases as the frequency is increased. While it may appear in Fig. 2 that $m_z(0; \omega_0 = 0.15) = 0$, in fact all conservative droplets with $0 < \omega_0 < 1$ satisfy $m_z(0; \omega_0) > -1$ owing to their nontopological structure.

The energy for the droplet $\mathcal{E}_0 \equiv \mathcal{E}[\Theta_0, (\omega_0 + h_0')t']$ satisfies[2,3]

$$\frac{d\mathcal{E}_0}{d\omega_0} < 0. \tag{11}$$

The fact that the energy is a decreasing function of frequency has been used to argue that the conservative droplet is stable in a 2D material.[3] The 2D conservative droplet embedded in an infinite, three-dimensional magnet is known to be unstable. However, preliminary studies suggest that, for sufficiently thin films, the 2D conservative droplet is stabilized. This work is beyond the scope of this paper and will appear elsewhere.

As we now show, the conservative droplet soliton can be generalized to damped/driven systems such as a nanocontact. Whenever we refer to "droplet," we mean the dissipative droplet studied in the future sections. We will always use "conservative droplet" to describe the solution of Eq. (8) that is monotonically decaying to zero as $\rho \to \infty$.

B. Dissipative droplet soliton

We now extend the analysis of Kosevich, Ivanov, and Kovalev[2,3] to the case of the dissipative droplet solution, where damping is no longer assumed to be negligible, and spin torque is included in the analysis. In addition to the balance between exchange and anisotropy that was required in the conservative droplet case, a further balance between uniform damping (loss) and spatially localized spin torque (gain) will be derived for the droplet to be sustained. We will assume that the spin torque and damping, while small, are not zero and are of the same magnitude so that

$$\sigma = \mathcal{O}(\alpha), \quad 0 < \alpha \ll 1.$$

We look for an asymptotic solution in the following form:

$$\Theta(\mathbf{r}', t') = \Theta_0(\rho'; \omega) + \alpha \Theta_1(\mathbf{r}', t') + \cdots,$$

$$\Phi(\mathbf{r}', t') = (\omega + h_0')t' + \alpha \frac{\Phi_1(\mathbf{r}', t')}{\sin \Theta_0(\rho'; \omega)} + \cdots. \tag{12}$$

We have set $\omega_0 \to \omega$ to distinguish the frequency of the droplet ω from that of the conservative droplet ω_0. We will conclude that there is no frequency shift due to damping and spin torque so that $\omega = \omega_0$ here. However, other perturbations beyond those considered here could lead to a frequency shift. Inserting the expansions in Eq. (12) into Eqs. (3) and (4), and equating like orders in α gives the following equations for the perturbations Θ_1 and Φ_1:

$$\frac{\partial \Theta_1}{\partial t'} + L_\Phi \Phi_1 = -(\omega + h_0')\sin \Theta_0$$

$$+ \frac{\sigma'}{\alpha} V(\rho') P_\Theta[\Theta_0, (\omega + h_0')t'], \tag{13}$$

$$\frac{\partial \Phi_1}{\partial t'} + L_\Theta \Theta_1 = -\frac{\sigma'}{\alpha} V(\rho') P_\Phi[\Theta_0, (\omega + h_0')t'], \tag{14}$$

where the self-adjoint, Schrödinger operators L_Φ and L_Θ are

$$L_\Phi \equiv -\frac{\delta F}{\delta \Phi}[\Theta_0, (\omega + h_0')t']\frac{1}{\sin \Theta_0}$$

$$= -\nabla'^2 - \left(\frac{d\Theta_0}{d\rho'}\right)^2 + \cos^2 \Theta_0 - \omega \cos \Theta_0,$$

$$L_\Theta \equiv \frac{\delta G}{\delta \Theta}[\Theta_0, (\omega + h_0')t'] - (\omega + h_0')\sin \Theta_0$$

$$= -\nabla'^2 + \cos 2\Theta_0 - \omega \cos \Theta_0.$$

Note the following important property:

$$L_\Phi \sin \Theta_0 = 0. \tag{15}$$

The rest of this section is concerned with the solution of the perturbative Eqs. (13) and (14) in two separate cases. We use standard solvability arguments for forced, linear differential equations to remove secular terms (see e.g., Ref. 19) in order to derive an expression for the current σ' at which the balancing condition for the droplet is achieved.

1. Case $\theta_f = 0$

We first consider the case where the fixed layer is oriented perfectly normal to the film plane so that $\theta_f = 0$. In this regime, we can study the effect of variable spin torque asymmetry ν.

In addition to the scalings in Eq. (5), we can also scale out the dependence on the applied field h_0' when $\theta_f = 0$ with the substitution

$$\Phi = \Phi' + h_0't'. \tag{16}$$

Then, Θ and Φ' satisfy Eqs. (3) and (4), as before, but with $h_0' = 0$. This transformation shows that the vertical applied field simply shifts the precessional frequency by h_0'.

We seek a solution to Eqs. (13) and (14) in the form $\theta_f = 0$, $h'_0 = 0$, $\Theta_1 \equiv 0$, and $\Phi'_1(\mathbf{r}',t') = \Phi'_1(\rho')$ (i.e., linear phase evolution with time) which results in the following nonhomogeneous equation for Φ'_1:

$$L_\Phi \Phi'_1 = -\omega \sin \Theta_0 + \frac{\sigma' V(\rho') \sin \Theta_0}{\alpha(1 + \nu \cos \Theta_0)},$$

$$\Phi'_1(0) = 0, \quad \frac{d\Phi'_1}{d\rho'}(0) = 0. \tag{17}$$

This equation is solvable if and only if the nonhomogeneous terms are orthogonal to the kernel of L_Φ. By use of Eq. (15), multiplying the right-hand side of Eq. (17) by $\rho \sin \Theta_0$ and integrating from 0 to infinity we obtain the existence condition for a dissipative droplet, $\sigma' = \sigma_{\text{sus}}(\omega)$, where

$$\sigma_{\text{sus}}(\omega) = \alpha\omega \frac{\int_0^\infty \sin^2 \Theta_0(\rho';\omega)\rho' d\rho'}{\int_0^\infty \frac{V(\rho')\sin^2 \Theta_0(\rho';\omega)}{1 + \nu \cos \Theta_0(\rho';\omega)}\rho' d\rho'}. \tag{18}$$

The choice $\sigma' = \sigma_{\text{sus}}(\omega)$ singles out a specific value for the current as a function of the droplet frequency $0 < \omega < 1$. This value of the current provides the necessary balance between damping and spin torque, in addition to the balance between exchange and anisotropy, in order to sustain the droplet. Therefore, we call $\sigma_{\text{sus}}(\omega)$ the *sustaining current*.

We can also understand the choice for the sustaining current in Eq. (18) by computing the rate of change in the energy for the droplet from Eq. (6)

$$\frac{d\mathcal{E}}{dt'}[\Theta_0, \omega t' + \alpha\Phi'_1/\sin \Theta_0]$$

$$= \omega \int_{\mathbb{R}^2}\left[\sigma_{\text{sus}}(\omega)V(\rho')\frac{\sin^2 \Theta_0}{1 + \nu \cos \Theta_0} - \alpha\omega \sin^2 \Theta_0\right]d\mathbf{r}'$$

$$+ \mathcal{O}(\alpha^2) = \mathcal{O}(\alpha^2). \tag{19}$$

Therefore, the energy of the droplet is approximately conserved for the choice $\sigma' = \sigma_{\text{sus}}$. Figure 3 shows a snapshot in time of a dissipative droplet.

Figure 4 represents the numerical evaluation of Eq. (18) and shows the dependence of σ_{sus} on ω. The droplet frequency has two branches as the sustaining current is varied but only one branch is stable. For a given droplet frequency ω, consider increasing the current slightly above the sustaining value, $\sigma' = \sigma_{\text{sus}}(\omega) + \delta\sigma'$. From Eq. (19), the droplet energy will increase, and from Eq. (11), this increase in energy corresponds to a *decrease* in droplet frequency for a stable droplet.[2,3] Thus, the upper branch in Fig. 4, for which increasing current causes an *increase* in frequency, is unstable.

Figure 4 shows that there is a minimum sustaining current $\sigma_{\text{sus}}^{\text{min}}$, maximum frequency ω^{max}, and maximum m_z in the center of the droplet m_z^{max} where

$$\sigma_{\text{sus}}^{\text{min}} \equiv \min_{\omega \in (0,1)} \sigma_{\text{sus}}(\omega) \equiv \sigma_{\text{sus}}(\omega^{\text{max}}),$$
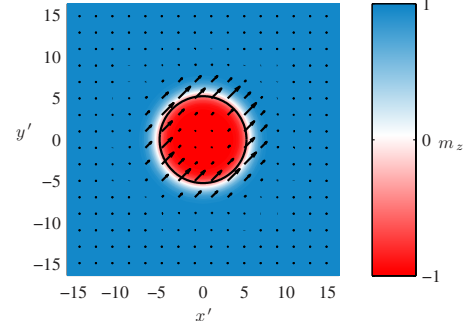

FIG. 3. (Color online) Dissipative droplet soliton for the high-symmetry case with $\theta_f = 0$. The color scale corresponds to m_z while the vector field corresponds to the in-plane components (m_x, m_y). The circle here and in future plots represents the boundary of the nanocontact. Parameters are $\sigma_{\text{sus}}/\alpha = 0.94$, $\omega = 0.17$, $\rho'_* = 5.24$, and $\nu = 0$.

$$m_z^{\text{max}} \equiv \cos \Theta_0(0; \omega^{\text{max}}).$$

While the specific choice of spin torque cut-off function $V(\rho')$ (e.g., we could have used a smooth cutoff, as opposed to a sharp, Heaviside cutoff) may be important in numerical applications,[20] it has only a slight effect on the droplet sustaining current. For the Heaviside cutoff considered here, Eq. (18) simplifies to

$$\sigma_{\text{sus}}(\omega) = \alpha\omega \frac{\int_0^\infty \sin^2 \Theta_0(\rho';\omega)\rho' d\rho'}{\int_0^{\rho'_*} \frac{\sin^2 \Theta_0(\rho';\omega)}{1 + \nu \cos \Theta_0(\rho';\omega)}\rho' d\rho'}. \tag{20}$$

Equation (20) reveals the explicit dependence of the sustaining current on two key spin torque parameters: the contact radius $\rho'_* > 0$ and the spin torque asymmetry $0 \le \nu < 1$. We now investigate properties of the dissipative droplet as a function of these two parameters. Figures 5(a)–5(d) show the dependence of $\sigma_{\text{sus}}^{\text{min}}$, m_z^{max}, ω^{max}, and the droplet radius ρ'_{drop} on the contact radius for various choices of the spin torque asymmetry. The droplet radius is defined to be the radius at half maximum
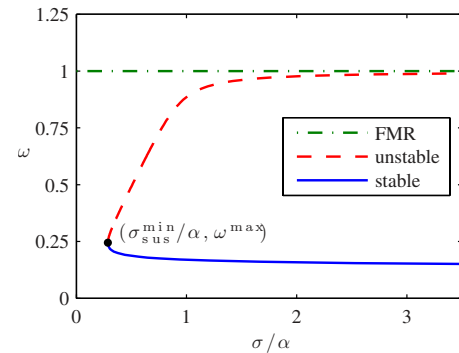

FIG. 4. (Color online) Dissipative droplet frequency (dashed and solid curves) as a function of sustaining current from Eq. (18). Parameters are $\rho'_* = 5.24$ and $\nu = 0$. The dashed-dotted line is the FMR frequency.
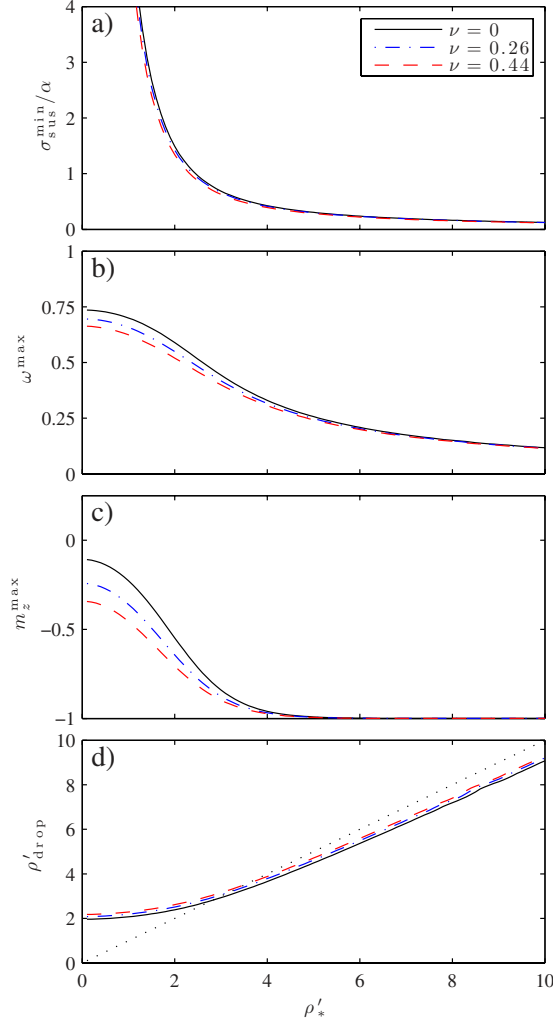
FIG. 5. (Color online) Dissipative droplet properties for varying contact radius ρ_*' and spin torque asymmetry ν: (a) minimum sustaining current, (b) maximum frequency, (c) maximum m_z at origin, and (d) droplet radius (dotted line is $\rho_{\text{drop}}' = \rho_*'$, plotted for comparison).

$$m_z(\rho_{\text{drop}}') = \frac{1}{2}(1 - m_z^{\text{max}}). \qquad (21)$$

Figure 5(a) shows that droplets excited by smaller contacts require larger sustaining currents. The dependence of $\sigma_{\text{sus}}/\alpha$ on ρ_*' and ν for small contact radii can be made explicit by an asymptotic evaluation of the denominator in Eq. (20) giving

$$\frac{\sigma_{\text{sus}}(\omega)}{\alpha} = \frac{2\omega[1 + \nu\cos\Theta_0(0;\omega)]\int_0^\infty \sin^2\Theta_0(\rho;\omega)\rho d\rho}{\rho_*'^2 \sin^2\Theta_0(0;\omega)}$$
$$+ \mathcal{O}(1), \quad 0 < \rho_*' \ll 1. \qquad (22)$$

Therefore, $\sigma_{\text{sus}}^{\text{min}}/\alpha$ grows like $1/\rho_*'^2$ for small contact radii in agreement with Fig. 5(a). Interestingly, we find that the droplet is constrained to have a frequency $0 < \omega \lesssim 0.75$ [Fig. 5(b)], significantly below the FMR frequency of 1. Also, since $m_z^{\text{max}} < 0$ [Fig. 5(c)], the droplet always has some re-

gion near its center that is partially inverted with respect to the surrounding magnetization. As shown in Fig. 5(d), the droplet is well localized within the nanocontact; e.g., $\rho_{\text{drop}}' < \rho_*'$, when $\rho_*' \gtrsim 3$. There is a minimum droplet radius of about $2\sqrt{h_k - 1}l_{\text{ex}}$ in dimensional units. Finally, spin torque asymmetry has only a small, perturbative effect and does not substantially alter the droplet solution.

2. Case $\nu = 0$

We consider now the case without spin torque asymmetry (i.e., $\nu = 0$) in which case we can study the effect of varying the angle of the fixed layer θ_{f} on the droplet dynamics. In this section, we use the rescalings in Eq. (5) but do not use the transformation in Eq. (16).

We solve Eqs. (13) and (14) with $\nu = 0$, $\Theta_1(\mathbf{r}', t') \equiv \Theta_s(\mathbf{r}')\sin\omega t'$, and $\Phi_1(\mathbf{r}', t') \equiv \widetilde{\Phi}(\mathbf{r}') + \Phi_c(\mathbf{r}')\cos\omega t'$, leading to the following system of nonhomogeneous equations:

$$L_\Phi\Phi_c + \omega\Theta_s = -\frac{\sigma'}{\alpha}\sin\theta_{\text{f}}V(\rho')\cos\Theta_0, \qquad (23)$$

$$L_\Theta\Theta_s - \omega\Phi_c = -\frac{\sigma'}{\alpha}\sin\theta_{\text{f}}V(\rho'), \qquad (24)$$

$$L_\Phi\widetilde{\Phi} = -(\omega + h_0')\sin\Theta_0 + \frac{\sigma'}{\alpha}\cos\theta_{\text{f}}V(\rho')\sin\Theta_0. \qquad (25)$$

Note that, in contrast to the case $\theta_{\text{f}} = 0$, the overall phase Φ no longer evolves linearly in time. Applying L_Θ to Eq. (23) and L_Φ to Eq. (24) gives the decoupled system

$$(L_\Theta L_\Phi + \omega^2)\Phi_c = \frac{\sigma'}{\alpha}\sin\theta_{\text{f}}[\omega V(\rho')$$
$$- L_\Theta\{V(\cdot)\cos\Theta_0(\cdot)\}(\rho')],$$

$$(L_\Phi L_\Theta + \omega^2)\Theta_s = \frac{\sigma'}{\alpha}\sin\theta_{\text{f}}[L_\Phi\{V(\cdot)\}(\rho')$$
$$- \omega V(\rho')\cos\Theta_0(\rho')].$$

These equations are always solvable if $L_\Theta L_\Phi + \omega^2$ and $L_\Phi L_\Theta + \omega^2$ are strictly positive operators. One can show that $L_\Phi \geq 0$, so that $L_\Phi L_\Theta + \omega^2 > 0$. One can also show that $L_\Theta \geq -\eta_\Theta^2$, where $-\eta_\Theta^2$ is the smallest eigenvalue of L_Θ and is strictly negative. Then, $L_\Theta L_\Phi \geq -\eta_\Theta^2$. We have verified by numerical computation of η_Θ that $\omega^2 > \eta_\Theta^2$ so that $L_\Theta L_\Phi + \omega^2 > 0$ as required, and Eqs. (23) and (24) are solvable.

We are interested in the solvability condition for $\widetilde{\Phi}$ in Eq. (25), which is

$$\sigma_{\mathrm{sus}}(\omega) = \alpha(\omega + h_0') \sec\theta_{\mathrm{f}} \frac{\displaystyle\int_0^\infty \sin\Theta_0(\rho';\omega)\rho'\,d\rho'}{\displaystyle\int_0^\infty V(\rho')\sin^2\Theta_0(\rho';\omega)\rho'\,d\rho'}.$$

$$(26)$$

Note that the applied field appears only as a shift in the droplet frequency, as in the case $\theta_{\mathrm{f}}=0$ studied in the previous section. The expression (26) for the sustaining current agrees with the previously derived sustaining current in Eq. (18) when $\nu=0$ and $\theta_{\mathrm{f}}=0$, as required. Thus, the dominant effect of rotating the fixed layer is to increase the sustaining current in proportion to $\sec\theta_{\mathrm{f}}$.

III. PHYSICAL PERTURBATIONS OF A DISSIPATIVE DROPLET

So far, we have considered the dissipative droplet solution only for a simplified geometry where asymptotic methods can be applied. In these cases, the external field is both uniform and oriented perfectly perpendicular to the film plane. By making this geometrical simplification, we were able to factor out the contribution of the external field from the droplet solution. However, in a real point-contact system, the external field is neither uniform nor perfectly perpendicular. In particular, the current flowing through the contact is an additional source of spatially inhomogeneous magnetic field, the Oersted field, and the applied uniform magnetic field in actual experiments is usually tilted away from the perpendicular axis. We employ micromagnetic simulations to investigate how these physically important perturbations to the external field alter the ideal droplet solution. The numerical details used for our simulations are presented in Appendix B

We find that the combination of external field tilt and the Oersted field breaks the symmetry of the solution such that the droplet is no longer centered in the middle of the contact. As a result, the solution takes on a nontrivial inhomogeneous phase structure where the phase of the spin precession closer to the center of the contact precedes the phase further from the center of the contact. In addition, the spatial structure of the droplet is no longer perfectly circular. For some particular combinations of simulation parameters, the droplet breaks away from the contact altogether and dissipates, a behavior we call a drift instability. When this occurs, the droplet may maintain its form for many precession cycles, but it eventually decays, since outside the contact there is no spin torque excitation to balance damping.

A. Oersted field

First, we consider the effect of the current-induced Oersted field while keeping the applied field and fixed layer oriented almost normal to the film plane (canted by 0.00001° and 0.40°, respectively). The reason for this slightly asymmetric configuration is to test whether high-symmetry solutions are structurally stable to small changes in the system parameters. Such a configuration is experimentally possible,
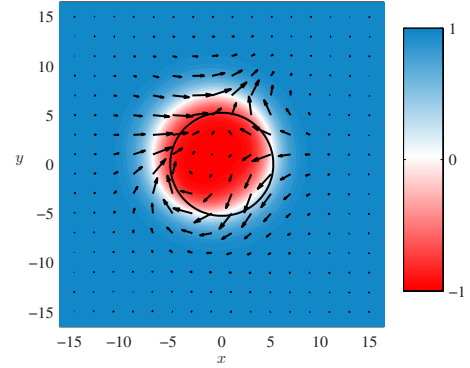

FIG. 6. (Color online) Dissipative droplet in the presence of the Oersted field and with the applied field and fixed layer nearly perpendicular to the plane. Parameter values are $h_k=1.25$, $\alpha=0.03$, $\rho_*=5.24$, $h_0=1.8$, $\theta_0=0.00001°$, $\theta_{\mathrm{f}}=0.40°$, $\nu=0.257$, and $\sigma=0.196$.

in principle. Our model for the Oersted field was presented in Ref. 18 and takes the form

$$\mathbf{h}_{\mathrm{oe}} = -f_{\mathrm{oe}}(\rho)\boldsymbol{\varphi},$$

where

$$f_{\mathrm{oe}}(\rho) = g_{\mathrm{oe}}(\rho) + \frac{I}{2\pi M_s r_*} \begin{cases} \rho/\rho_* & 0 < \rho < \rho_* \\ \rho_*/\rho & \rho_* < \rho. \end{cases} \quad (27)$$

The function $g(\rho)$ given in Ref. 18 involves integrals of Bessel functions and depends on the geometry of the current-density distribution. The parameters defining g in Ref. 18 are $d=1.67$, $z_*=-0.925$, and $a=2.92$. The other, more dominant, term in Eq. (27) is the field generated by an infinitely long conducting wire. As an example, for the simulation in Fig. 6,
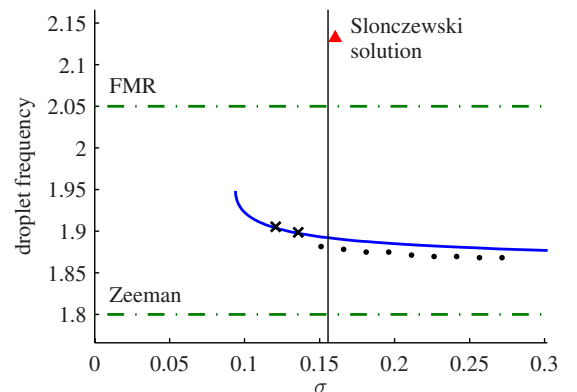

FIG. 7. (Color online) Dots: perturbed droplet frequency as a function of current with the Oersted field computed from micromagnetic simulations. Crosses: perturbed droplets that undergo a drift instability; the frequency is calculated before the instability manifests. Solid curve: droplet frequency as a function of the sustaining current from Eq. (20). Dashed-dotted: the Zeeman (h_0) and FMR (h_0+h_k-1) frequencies. Triangle: the Slonczewski critical current and onset frequency for high-symmetry (Ref. 8) (see Appendix A). Solid vertical line: numerically computed threshold current in the presence of the Oersted field and the canted fixed layer. Parameter values are the same as in Fig. 6.
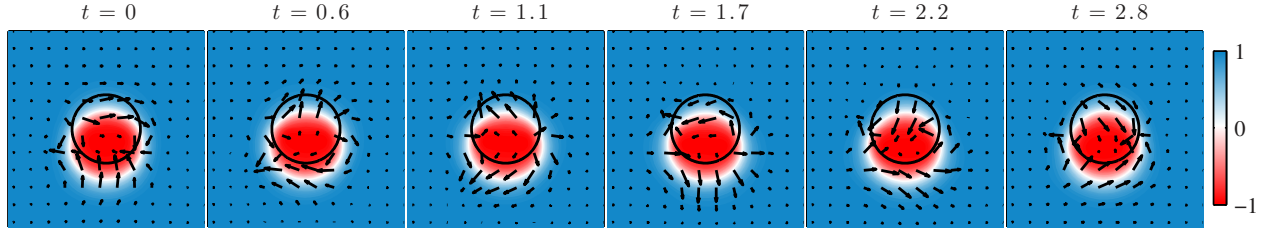
FIG. 8. (Color online) Time sequence of a strongly perturbed droplet over one period of precession in the presence of a canted applied field, canted fixed layer, and Oersted field. Parameter values are h_k=1.25, α=0.03, ρ_*=5.24, h_0=1.8, θ_0=5°, θ_f=31.4°, ν=0.257, and σ=0.189. The time of the initial panel here and in Fig. 9 is set to 0 for comparison. The simulation actually began earlier.

we have $\max_{\rho \in [0,\infty]} |g_{oe}(\rho)|$=0.0081, while $I/2\pi M_s r_*$=0.086, an order of magnitude difference.

Figure 6 illustrates how the Oersted field changes the structure of the droplet. In contrast with the symmetric case in Fig. 3, the azimuthal angle Φ shows significant spatial variations. The droplet is also slightly shifted off-center. The strong phase variations are indicative of a tendency for the droplet to propagate.[21] In some cases, although not for the simulation in Fig. 6, the droplet breaks free from the nano-contact. This drift instability is discussed further in Sec. III B.

In Fig. 7 we compare the numerically computed perturbed droplet frequency as a function of current with the sustaining current from Eq. (20). We find that the droplet frequency is approximately shifted down by an overall amount of 0.012 but otherwise follows the same trend as the symmetric result. This behavior demonstrates that the analysis of the previous section, despite the necessary high-symmetry restrictions, yields relevant, qualitative information about localized structures excited in a physically realizable nanocontact.

As will be shown in Sec. IV, when the current exceeds a threshold value; e.g., the Slonczewski critical current,[8] a droplet can nucleate for sufficiently large anisotropy. The vertical line in Fig. 7 is the numerically computed threshold current. It differs from Slonczewski's result because $\mathbf{h}_{oe} \neq 0$, $\theta_0 > 0$, and $\theta_f > 0$. This threshold for droplet nucleation suggests a hysteretic effect that will be discussed in Sec. IV C.

Our micromagnetic simulations also show that the perturbed droplet, for certain parameter choices (e.g., the crosses in Fig. 7), undergoes a drift instability. This behavior will now be investigated further.

B. Canted applied field, fixed layer, and Oersted field

In this section, we investigate the combined effects of the Oersted field as well as canting of the applied field and fixed

layer. Figure 8 is a time sequence showing the evolution of a strongly perturbed droplet over one precessional period. In contrast to the nearly symmetric configuration of Fig. 6, where the droplet was slightly shifted to the left, the droplet is slightly shifted down, toward the region of lower in-plane field.

As the system parameters are changed, the shifting of the droplet center can be large enough to actually dislodge the droplet from the nanocontact. An example of this drift instability is shown in the panels of Fig. 9. The current was taken to be less than the current for Fig. 8, which did not experience a drift instability. A number of precessional periods pass before the droplet breaks free. Once free, it propagates, but because it no longer satisfies the required balancing condition between damping and spin torque, it loses amplitude and decays. Once the droplet has drifted outside of the nanocontact, a new one is formed if the nucleation conditions are satisfied (see Sec. IV). We have also observed droplets that drift several nanocontact diameters before decaying, i.e., the central magnetization lifts up so that $\min_{\mathbf{r} \in \mathbb{R}^2} m_z(\mathbf{r},t) > 0$. The manifold in parameter space in which the droplet manifests a drift instability appears to be complicated. Nevertheless, we readily find parameter regimes where the droplet apparently does not experience the drift instability, as in Figs. 6–8.

Notice that the drifting droplet of Fig. 9 propagates down, in the $-\mathbf{y}$ direction. Recall that the canting direction of the applied field is along $\mathbf{x}$. Due to the symmetry of the Oersted field, the direction of propagation of the drifting droplet appears to track the azimuthal angle of the applied field minus 90°, if θ_0 is sufficiently large. For example, if the applied field is canted along $\mathbf{y}$, then the droplet will drift along $\mathbf{x}$ if unstable. This can be understood as a consequence of magnetostatic interactions between the effective dipole moment of the droplet and the field gradient associated with the Oersted field. Given the canting of the applied field, the effective
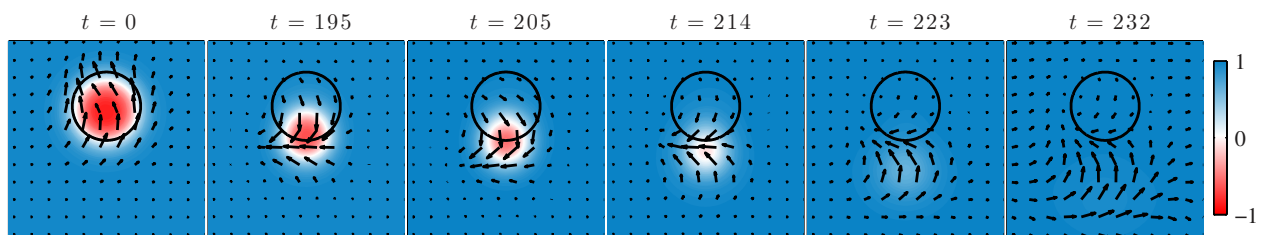

FIG. 9. (Color online) Time sequence showing the droplet drift instability for the same parameter values as in Fig. 8 but with smaller current σ=0.121. To facilitate visualization, the length of the in-plane magnetization vectors is normalized to the largest value in each frame.
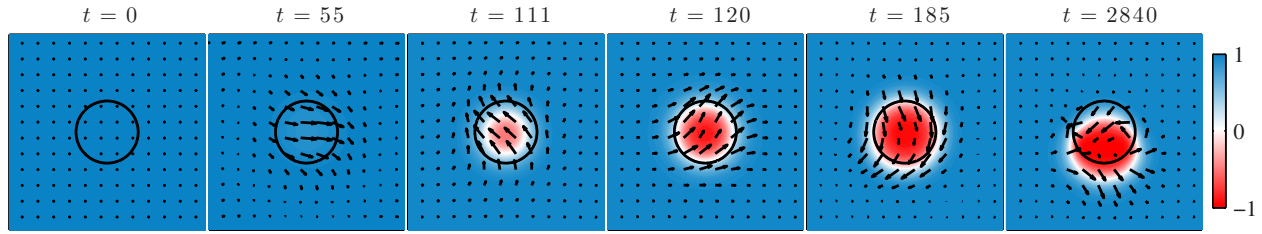
FIG. 10. (Color online) Birth of a dissipative droplet soliton for the current $\sigma = 0.186$, above the Slonczewski critical current $\sigma_{\rm s} = 0.160$. Parameter values are the same as those in Fig. 8.

dipole moment of the droplet acquires an in-plane component that is drawn to the edge of the contact where the Oersted field is also in the $-\mathbf{x}$ direction such that the Oersted field gradient acts to trap the droplet. In the case of Fig. 6, where the applied field is canted only $0.00001°$, the droplet is observed to drift to the left rather than down. Therefore, the strength of the Oersted field and the in-plane component of the applied field have a strong effect on the existence and dynamics of a drift instability.

IV. NUCLEATION OF A DISSIPATIVE DROPLET

Figure 10 shows the birth of the droplet pictured in Fig. 8 starting from a state pointing uniformly in the $\mathbf{z}$ direction. For sufficiently large perpendicular anisotropy h_k and current, the magnetization inside the nanocontact reverses and nucleates a droplet. In this section we show that the reversal mechanism is caused by an instability of small amplitude waves. We will study Eq. (1) in the weakly nonlinear regime and find that the small amplitude Slonczewski mode that exists near the threshold for the onset of dynamics is stable/unstable depending on whether h_k is less than/greater than a critical value $h_k^{\rm cr}$. We find that $h_k^{\rm cr} > 1$ due to exchange effects and converges to 1 as the contact size is increased. The value of $h_k^{\rm cr}$ is important for the possible experimental observation of a dissipative droplet.

A. Stability analysis of a macrospin

Before studying the partial differential equation (PDE) in Eq. (1), we consider the macrospin model where spatial variation is neglected. The stability analysis for this model is suggestive and mathematically simpler. However, we find that the critical anisotropy field in the macrospin case $h_k^{\rm cr,m}$ satisfies $h_k^{\rm cr,m} \leq 1$ and depends strongly on the applied field, which differs from the result obtained by analyzing the full PDE model, where we find $h_k^{\rm cr} > 1$ with weak applied field dependence.

We consider Eqs. (3) and (4) neglecting all spatial variation and interlayer dipole coupling in the symmetric regime $\theta_0 = 0$ and $\theta_f = 0$; i.e., we are assuming that the initial condition for the system is in the parallel state. In this case, the equation for Θ is decoupled from Φ, so we can just study the scalar, first-order ordinary differential equation

$$\dot{\Theta} = -\alpha \sin \Theta [\cos \Theta (h_k - 1) + h_0] + \frac{\sigma \sin \Theta}{1 + \nu \cos \Theta}. \quad (28)$$

By linearizing Eq. (28) about the equilibrium $\Theta \equiv 0$, we find that it becomes unstable when

$$\sigma > \sigma_0 \equiv \alpha(1 + \nu)(h_0 + h_k - 1),$$

in agreement with previous numerical and mathematical analyses of this system contained in Ref. 22. We seek a periodic equilibrium solution $\Theta(t) = \Theta_{\rm e}$ just above threshold by taking

$$\sigma = \sigma_0 + \varepsilon, \quad 0 < \varepsilon \ll \sigma_0.$$

Then, from Eq. (28)

$$\Theta_{\rm e} \sim \left\{ \frac{2\alpha\varepsilon}{1 - h_k + \nu[2(1 - h_k) - h_0]} \right\}^{1/2}.$$

This solution exists (is real valued) as long as

$$h_k < h_k^{\rm cr,m} \equiv 1 - \frac{\nu h_0}{1 + 2\nu} < 1. \quad (29)$$

Furthermore, one can show that this equilibrium is stable. Therefore, when $h_k < h_k^{\rm cr,m}$, the equilibrium $\Theta \equiv 0$ undergoes a supercritical Hopf bifurcation as the current σ is increased beyond σ_0. When $h_k > h_k^{\rm cr,m}$, there is no periodic solution, and the system switches from $\Theta \equiv 0$ to the fully reversed state $\Theta_{\rm e} = \pi$ when σ exceeds σ_0.

B. Stability analysis of the micromagnetic system

We consider Eq. (1) in the symmetric regime with $\theta_0 = 0$, $\mathbf{h}_{\rm oe} \equiv 0$, $\theta_f = 0$, and the substitutions

$$u = m_x + im_y, \quad m_z = \sqrt{1 - |u|^2} \sim 1 - \frac{1}{2}|u|^2,$$

where $|u| \ll 1$. Then u approximately satisfies a complex nonlinear Schrödinger-type equation

$$i\frac{\partial u}{\partial t} = (1 + i\alpha)\nabla^2 u - (h_0 + h_k - 1)u - i\alpha(h_0 + h_k - 1)u$$

$$+ i\frac{\sigma V(\rho)}{1 + \nu}u + \frac{1}{2}(h_k - 1)|u|^2 u + \frac{1}{2}(u\nabla^2|u|^2 - |u|^2\nabla^2 u)$$

$$+ i\alpha|\nabla u|^2 u + \frac{i}{2}\left[\alpha(h_0 + 2h_k - 2) - \frac{\sigma V(\rho)}{(1 + \nu)^2}\right]|u|^2 u. \quad (30)$$

Similar to the macrospin case, when σ is increased past a threshold value, the zero solution becomes unstable. The threshold, critical current and onset frequency were found by Slonczewski as a solution to a linear eigenvalue problem[9]

[see Eq. (A1)]. Incorporating weak nonlinear effects, Ref. 23 showed that a small amplitude periodic solution exists as a modulation of the Slonczewski mode for $h_k=0$ and $\nu=0$. This time-periodic, weakly nonlinear mode was found to be numerically stable. In this section and Appendix A, we extend these results to $0 \leq h_k < h_k^{\mathrm{cr}}$ and $0 \leq \nu < 1$, where h_k^{cr} is defined through $\mathrm{Im}[\xi(h_k^{\mathrm{cr}})]=0$ and ξ is given by Eq. (A4). This behavior is analogous to the supercritical Hopf bifurcation for the macrospin, studied in the previous section.

In this section, we show that weakly nonlinear modulations of the Slonczewski mode are no longer stable when $h_k > h_k^{\mathrm{cr}} > 1$. This behavior is analogous to the switching exhibited by the macrospin for $h_k > h_k^{\mathrm{cr,m}}$ and σ above threshold. While we are unable to analytically follow the dynamics of the instability, numerical simulations such as the droplet birth sequence shown in Fig. 10 demonstrate that the magnetization reverses inside the nanocontact and develops into a dissipative droplet.

For the stability analysis, we seek a multiple scales solution representing a modulation of the Slonczewski mode in the form

$$u(\mathbf{r},t) = e^{i(h_0+h_k-1)t} e^{i\omega_s t} [\varepsilon A(T) f(\rho) + \varepsilon^3 u_1(\mathbf{r},T) + \cdots],$$

$$\sigma = \sigma_s + \varepsilon^2 \sigma_1, \tag{31}$$

where $0 < \varepsilon \ll 1$ is the amplitude of the mode at the origin, which is modulated by $A(T)$ with $T=\varepsilon^2 t$ the "slow" time, ω_s is the frequency of the Slonczewski mode $f(\rho)$ with threshold current σ_s, and σ_1 represents a deviation from σ_s. The explicit form for f and the implicit equations for ω_s and σ_s are given in Appendix A.

Invoking a solvability condition at $\mathcal{O}(\varepsilon^3)$, Eq. (A3) gives the nonlinear amplitude equation

$$i \frac{dA}{dT} = i \frac{\sigma_1}{1+\nu} \zeta A + \xi |A|^2 A \tag{32}$$

with complex linear and nonlinear coefficients ζ and ξ. There is a time-periodic solution of Eq. (32) for a specific choice of $\sigma_1 \in \mathbb{R}$

$$A(T) = e^{i\omega_{s,1}T}, \quad \sigma_1 = -(1+\nu)\frac{\mathrm{Im}(\xi)}{\mathrm{Re}(\zeta)},$$

$$\omega_{s,1} = -\mathrm{Re}(\xi) - \frac{\mathrm{Im}(\xi)\mathrm{Im}(\zeta)}{\mathrm{Re}(\zeta)}. \tag{33}$$

This solution represents the nonlinear frequency shift $\varepsilon^2 \omega_{s,1}$ to the Slonczewski frequency ω_s. The stability analysis in A shows that the solution (33) is unstable when $\mathrm{Im}(\xi)>0$. An explicit formula for ξ is given in Eq. (A4). We evaluate the integrals numerically and plot $\mathrm{Im}(\xi)$ as a function of h_k for specific parameter values in Fig. 11.

There is a critical value of the anisotropy field h_k^{cr} satisfying

$$\mathrm{Im}[\xi(h_k^{\mathrm{cr}})] = 0 \tag{34}$$

above which the weakly nonlinear Slonczewski mode is modulationally unstable. In other words, weak modulations of the Slonczewski mode will grow exponentially in time
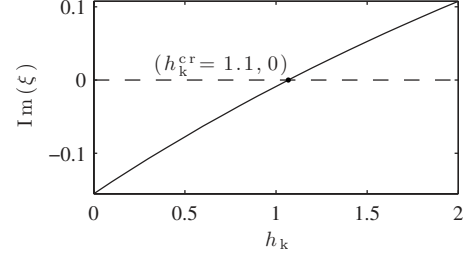

FIG. 11. Modulation parameter $\mathrm{Im}(\xi)$ as a function of h_k. When $\mathrm{Im}(\xi)>0$, the weakly nonlinear Slonczewski mode is modulationally unstable. Parameter values are $\alpha=0.03$, $\rho_*=5.24$, $h_0=1.8$, and $\nu=0.26$.

when $h_k > h_k^{\mathrm{cr}}$. Figure 12 shows the dependence of $h_k^{\mathrm{cr}} = h_k^{\mathrm{cr}}(\rho_*, \nu, h_0)$, computed numerically by solving Eq. (34) with Eq. (A4), as the contact radius and spin torque asymmetry are varied and $h_0=1.8$. We see that h_k^{cr} is strictly greater than one and that larger perpendicular anisotropy is required to enable the nucleation of a droplet in smaller nanocontact devices. For a given contact size, larger spin torque asymmetry permits nucleation of a droplet at smaller values of h_k.

We have also investigated the dependence of h_k^{cr} on the applied field magnitude h_0. Since h_0 appears in ξ only multiplied by α, we have $\frac{\partial}{\partial h_0} h_k^{\mathrm{cr}}(\rho_*, \nu, h_0) = \mathcal{O}(\alpha)$, which is small. This is confirmed by numerical calculations of the h_k^{cr} dependence on $h_0 \geq 0$ for the values of ρ_* and ν plotted in Fig. 12. We find that h_k^{cr} varies by at most 3% for $h_0 \in [0, 1.8]$ with $\frac{\partial}{\partial h_0} h_k^{\mathrm{cr}}(\rho_*, \nu, h_0) < 0$. Importantly, the lower bound for h_k^{cr} is preserved: $h_k^{\mathrm{cr}}(\rho_*, \nu, h_0) > 1$ when $h_0 \geq 0$. This behavior stands in stark contrast to the macrospin result for $h_k^{\mathrm{cr,m}} < 1$ in Eq. (29) that strongly depends on the applied field.

From Eq. (33), we see that σ_1 is negative when $\mathrm{Im}(\xi)/\mathrm{Re}(\zeta) > 0$. Numerically, we find that $\mathrm{Re}(\zeta) > 0$, so that $\sigma_1 < 0$ when $h_k > h_k^{\mathrm{cr}}$, which corresponds precisely to the instability criterion. Furthermore, when $\sigma_1 < 0$, any finite-amplitude excitation will tend to grow, thus the time-periodic solution is unstable. This behavior is similar to the macrospin model discussed in the previous section where, for $h_k > h_k^{\mathrm{cr}}$, a small amplitude periodic solution did not exist.

Numerical simulations of Eq. (1) confirm the foregoing analysis, even in the nonsymmetric cases with $\theta_0 > 0$, $\theta_f > 0$, and $\mathbf{h}_{\mathrm{oe}} \neq 0$. There is a critical value of the current above
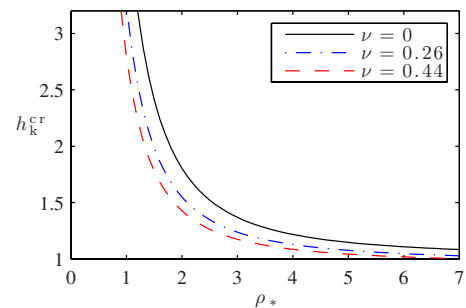

FIG. 12. (Color online) The critical anisotropy field h_k^{cr} as a function of contact radius ρ_* for various spin torque asymmetries ν. Other parameters are $\alpha=0.03$ and $h_0=1.8$.

which large amplitude dynamics ensue. When h_k is above h_k^{cr}, we find that the magnetization inside the nanocontact reverses to form a localized, coherently precessing, fully nonlinear magnetic solitary wave. We identify this solitary wave with the dissipative droplet soliton found in the asymptotic analysis of Sec. II.

Due to the numerically robust formation of the droplet for a variety of initial data and across a large parameter regime, we view it as a global attractor. As long as the current is above threshold, a droplet is observed to nucleate.

C. Hysteresis

We have shown in this section that a dissipative droplet will form when the current exceeds the threshold for instability of small amplitude waves inside the contact. In the high-symmetry case of Eq. (2) and $\theta_f = 0$, the threshold is the Slonczewski critical current σ_s, which is plotted in Fig. 7 (triangle) along with the numerically calculated threshold current from micromagnetic simulations that incorporate the Oersted field and a canted fixed layer ($\sigma = 0.156$, vertical line). We observe that the minimum droplet sustaining current is below the threshold for droplet nucleation. This suggests a hysteretic effect, whereby a droplet can be nucleated at a current above threshold and remains stable when followed by an adiabatic decrease in the current below threshold. We have performed this experiment numerically for the perturbed droplets of Fig. 7. We use an already nucleated droplet (at $\sigma = 0.211$) as the initial condition for a new simulation with $\sigma = 0.151$, below threshold. We find that sufficiently close to, but below, threshold, the droplet's frequency slightly increases but remains stable. For further decrease of the current to $\sigma = 0.136$, however, the droplet undergoes a drift instability similar to behavior shown in Fig. 9. Since the current is below threshold a new droplet does not form.

V. DISCUSSION

The Slonczewski form for the spin torque term we are considering here, Eq. (1), was derived strictly for the case of spatially uniform magnetization distributions.[6] Nonlocal generalizations of the spin torque term to nonuniform magnetization distributions have been derived in the small amplitude regime[24] and applied to single layer nanocontact simulations.[18] Because the spin torque and damping terms are treated as perturbations giving rise to a dissipative droplet solution, we expect that the specific form for the spin torque term, and the damping term for that matter, will not yield qualitative changes in the structure of the droplet. The asymptotic analysis presented here is applicable to an arbitrary spin torque term as long as its net effect is to oppose the inherent damping in the system.

Due to the symmetries in the problem when $\theta_0 = \theta_f \approx 0$, one might expect the Oersted field to prefer the excitation of a localized vortex structure; e.g., a topological soliton.[3] We observe no such excitations in our simulations.

Two-dimensional, conservative topological solitons are stable but they have higher energy than the conservative nontopological soliton,[3] providing one possible explanation for this behavior. Another possible explanation lies in the form of the spin torque term. In contrast to the *local* form for the spin torque considered here, single-layer nanocontact simulations that incorporate a *nonlocal* spin torque have demonstrated the formation and numerical stability of a precessional vortex in high-symmetry configurations without perpendicular anisotropy.[18] A more realistic model of the spin torque may favor a topological soliton in certain cases.

Unfortunately, we as yet have no detailed physical understanding of either the dissipative droplet asymmetry or the drift instability in the presence of the combined effects of an Oersted field and a tilted applied field. In part, our lack of understanding stems from the limited theory for the spatial propagation of the droplet.[21,25] Extension of the theory presented here to cases where the droplet is accelerated by field gradients and other such forces may provide more physical insight to aid in understanding why the droplet is subjected to displacing forces.

The physical appearance of the droplet is reminiscent of the magnetic bubble that was once the subject of intense investigation as a possible alternative to ferrite-core computer memory.[15] Indeed, we can identify the zero-frequency droplet as a topologically trivial magnetic bubble[26] with a winding number of zero, though in the theory presented here, the droplet frequency approaches zero only in the limit of infinitely large diameter. However, we expect that the droplet will converge to the bubble structure at a finite diameter, contingent on the inclusion of nonlocal magnetostatic energy in the calculation; even when considering free layer films as thin as 3 nm, such a term will eventually overcome the positive contribution of exchange energy to the oscillator frequency, stabilizing the droplet as a static structure. In this sense, then, we can think of the conservative droplet soliton, a delicate balance between exchange and perpendicular anisotropy, as a dynamically collapsing bubble, and the dissipative droplet soliton as an imminently collapsing bubble that is critically stabilized by the localized injection of spin torque.

VI. CONCLUSION

We have derived equations for a dissipative droplet soliton through an asymptotic analysis of the Landau-Lifshitz-Slonczewski equation for a point-contact spin torque oscillator with perpendicular anisotropy in the free layer. The droplet soliton is a localized, dynamic, solitary wave solution consisting of partially reversed magnetization directly under the contact and a zone of large amplitude precession in a region bounding the reversed magnetization. The diameter of the precessing boundary is approximately the contact diameter. The droplet frequency is always strictly less than the ferromagnetic resonance frequency for the film and is also a monotonically decreasing function of droplet diameter. The

balance between spin torque and damping required to sustain the droplet determines the relation between bias current and frequency. The instability of small amplitude solutions that leads to formation of the reversed domain in the droplet requires a minimum perpendicular anisotropy that is a function of the contact radius and spin torque asymmetry.

Some of the unique, identifying properties of the dissipative droplet that could be observed experimentally include (a) the droplet's frequency is well below the ferromagnetic resonance frequency. (b) Sufficiently far from the minimum sustaining current, the droplet's frequency has a weak dependence on current. (c) The droplet may manifest a drift instability, which would reveal itself as a transitory cessation in ac oscillations until the droplet again forms. (d) Hysteresis in current is expected, unless a drift instability results in a finite droplet lifetime.

We have investigated the nucleation and stability of the dissipative droplet soliton through numerical simulations. We find that droplet formation begins once the current in the point contact is sufficient to instigate the small amplitude Slonczewski mode, characterized by spin waves that radiate away from the point contact. For sufficiently strong perpendicular anisotropy, this mode is subject to a modulational instability and rapidly evolves into the reversed magnetization profile of the droplet soliton. We find that the droplet is stable in certain parameter regimes with regard to the inhomogeneous Oersted field and to variations in spin torque asymmetry and applied field angle. Finally, the droplet is subject to a drift instability that is a complicated function of the parameters employed in this theory.

APPENDIX A: MODULATIONAL INSTABILITY OF SLONCZEWSKI MODE

Here we provide the details of our stability analysis for small amplitude, modulated waves excited in a nanocontact. Inserting the ansatz in Eq. (31) into Eq. (30) and considering the leading order behavior in ε gives the linear Slonczewski eigenmode $f(\rho)$ satisfying[8]

$$L_0 f \equiv (1 + i\alpha)\left(f'' + \frac{1}{\rho}f'\right) - i\alpha(h_0 + h_k - 1)f + i\frac{\sigma_s V(\rho)}{1+\nu}f + \omega_s f$$

$$= 0. \tag{A1}$$

Slonczewski considered both ω_s and σ_s as eigenvalues for this equation and found the $C^1[0, \infty)$ solution

$$f(\rho) = \begin{cases} J_0(k_i\rho) & 0 \le \rho \le \rho_* \\ cH_0^{(1)}(k_o\rho) & \rho_* < \rho \end{cases}, \quad c = \frac{J_0(k_i\rho_*)}{H_0^{(1)}(k_o\rho_*)},$$

where J_0 is a Bessel function and $H_0^{(1)}$ is a Hankel function. The inner and outer wave numbers k_i and k_o are

$$k_i = \sqrt{\frac{\omega_s - i[\alpha(h_0 + h_k - 1) - \sigma_s/(1+\nu)]}{1 + i\alpha}},$$

$$k_o = -\sqrt{\frac{\omega_s - i\alpha(h_0 + h_k - 1)}{1 + i\alpha}}.$$

Since $|f(\rho)| \sim Ce^{-\text{Im}(k_o)\rho}/\sqrt{\rho}$ for $\rho \gg \rho_*$, the sign of k_o has been chosen so that $\text{Im}(k_o) > 0$, and f experiences exponential decay due to material damping $\alpha > 0$. The decay length is weak compared to the contact radius. The two real eigenvalues ω_s and σ_s are determined by solving the complex valued transcendental equation

$$k_i H_0^{(1)}(k_o\rho_*)J_1(k_i\rho_*) = k_o H_1^{(1)}(k_o\rho_*)J_0(k_i\rho_*),$$

which results from continuity of the first derivative of f.

Continuing the asymptotic analysis to the next order gives the following nonhomogeneous equation:

$$L_0 u_1 = R_1 \equiv -i\frac{dA}{dT}f + i\frac{\sigma_1 V(\rho)}{1+\nu}Af + \frac{1}{2}|A|^2A\left\{\left[h_k - 1 + i\alpha(h_0\right.\right.$$

$$+ h_k - 1) - i\frac{\sigma_s V(\rho)}{(1+\nu)^2}\right]|f|^2f + f\left[\frac{d^2}{d\rho^2} + \frac{1}{\rho}\frac{d}{d\rho}\right]|f|^2$$

$$- |f|^2\left[f'' + \frac{1}{\rho}f'\right] + 2i\alpha|f'|^2f\right\}. \tag{A2}$$

Since the kernel of the adjoint of L_0 is spanned by f^* (* denotes complex conjugation), we invoke the solvability condition of Eq. (A2)

$$\int_0^\infty f(\rho)R_1(\rho)\rho d\rho = 0 \tag{A3}$$

to determine the dynamical equation for $A(T)$ in Eq. (32). The complex valued linear and nonlinear coefficients ζ and ξ are

$$\zeta = \frac{1 + [J_0(k_i\rho_*)/J_1(k_i\rho_*)]^2}{1 - [k_i/k_o]^2}$$

and

$$\xi = \frac{[h_k - 1 + i\alpha(h_0 + h_k - 1)]\int_0^\infty |f|^2f^2\rho d\rho - i\frac{\sigma_s}{(1+\nu)^2}\int_0^{\rho_*} |f|^2f^2\rho d\rho - (1 - 2i\alpha)\int_0^\infty |f'|^2f^2\rho d\rho}{\rho_*^2 J_1(k_i\rho_*)^2[1 - (k_i/k_o)^2]}. \tag{A4}$$

We now perform a linear stability analysis of the time-periodic solution $A(T) = e^{i\omega_{s,1}T}$ in Eq. (33) by inserting

$$A(T) = e^{i\omega_{s,1}T}(1 + v + iw), \quad v, w \in \mathbb{R}, \quad |v|, |w| \ll 1$$

into Eq. (32). Keeping only the terms linear in v and w gives the simple, decoupled dynamical system

$$\frac{dv}{dT} = 2\,\mathrm{Im}(\xi)v, \quad \frac{dw}{dT} = -2\,\mathrm{Re}(\xi)v,$$

which experiences exponential growth when $\mathrm{Im}(\xi) > 0$.

APPENDIX B: MICROMAGNETIC COMPUTATIONAL MODELING

The numerical method we have used to solve Eq. (1) is similar to the method tersely presented in Ref. 18 but adapted to a trilayer nanocontact. In this appendix, we describe our method in detail. In brief, we use a polar coordinate grid and cylindrical magnetization basis. Angular derivatives are computed by use of a pseudospectral, Fourier method while radial derivatives on a nonuniform grid are computed by use of finite differences. For time stepping, we use an explicit, hybrid second-order Runge-Kutta time stepper with error control, ODE23 from Matlab®.

The polar coordinate system is a particularly efficient and accurate choice for nanocontact simulations. The discretization we use is nonuniform in radius ("inner" and "outer" grids)

$$\rho_n = q(n)$$
$$\equiv \rho_* \int_0^n \left\{ (d\rho_{\mathrm{out}} - d\rho_{\mathrm{in}}) \left[\tanh\left(\frac{\xi - \hat{n}}{w} \right) + 1 \right] + d\rho_{\mathrm{in}} \right\} d\xi,$$
$$(B1)$$

where $n = 1, \dots, N$, and $\hat{n}$, w are parameters determining the location and width of the smooth change from the fine inner grid spacing $d\rho_{\mathrm{in}}$ to the coarser outer grid spacing $d\rho_{\mathrm{out}} > d\rho_{\mathrm{in}}$. We typically have $\rho_1 \approx d\rho_{\mathrm{in}}$. For the angular, pseudospectral discretization, we expand the cylindrical magnetization basis in a truncated Fourier series with M Fourier modes

$$\mathbf{m}(\rho_n, \varphi, t) \approx \sum_{k=-M/2}^{M/2-1} e^{ik\varphi} [\hat{m}_{n,k}^{(\rho)}(t)\boldsymbol{\rho} + \hat{m}_{n,k}^{(\varphi)}(t)\boldsymbol{\varphi} + \hat{m}_{n,k}^{(z)}(t)\mathbf{z}].$$
$$(B2)$$

The transformation from an equispaced angular grid $\varphi_k = -\pi + (k-1)2\pi/M$ with magnetization coefficients $m_{n,k}^{(\rho,\varphi,z)}(t)$ evaluated at the discrete grid (ρ_n, φ_k), to the Fourier representation in Eq. (B2) is achieved by use of the fast Fourier transform.

The advantage of this discretization is that we can solve on a uniform computational grid while the physical grid is clustered in and around the nanocontact, where the majority of the fine scale dynamics occur. The outer grid supports the propagation of spin waves of the appropriate wavelength away from the nanocontact. In order to simulate an infinite domain, we choose a finite domain large enough, $L \equiv \rho_N$

$\approx 30\rho_*$, so that spurious waves are naturally damped to a negligible amplitude. Then their reflection off the boundary does not affect the strongly localized dynamics near the nanocontact.

Computing the vector Laplacian $\nabla^2 \mathbf{m}$ is the computationally intensive portion of the algorithm. Angular derivatives are approximated by multiplication in Fourier space $\frac{\partial}{\partial \varphi} \to ik$. The approximation of radial derivatives using finite differences requires some care, especially near the origin. We discuss the details now.

Due to the nonuniform radial grid in Eq. (B1), radial derivatives in computational space require appropriate factors of q and its derivatives. For example,

$$\frac{\partial}{\partial \rho} \to \frac{1}{q'}\frac{\partial}{\partial n}, \quad \frac{\partial^2}{\partial \rho^2} \to \frac{1}{q'^3}\left(q'\frac{\partial^2}{\partial n^2} - q''\frac{\partial}{\partial n} \right).$$

The radial derivatives in computational space are approximated using sixth-order finite differences. The boundary condition at the artificial boundary $\rho = L$ for Eq. (1) is the Neumann condition $\frac{\partial \hat{m}_N^{(\rho,\varphi,z)}}{\partial \rho}(t) = 0$, which is implemented by use of a standard ghost point method and one-sided differences. For radial derivatives near the origin at $n = 1, 2$, we define symmetry conditions to obtain $\hat{m}_{-n,k}^{(\rho,\varphi,z)}(t)$ by taking $\varphi \to \varphi + \pi$

$$\hat{m}_{n,k}^{(\rho)}(t)e^{ik\varphi}\boldsymbol{\rho} = (-1)^{k+1}\hat{m}_{n,k}^{(\rho)}(t)e^{ik(\varphi+\pi)}(-\boldsymbol{\rho})$$
$$\equiv (-1)^{k+1}\hat{m}_{-n,k}^{(\rho)}(t)e^{ik\varphi}\boldsymbol{\rho},$$

$$\hat{m}_{n,k}^{(\varphi)}(t)e^{ik\varphi}\boldsymbol{\varphi} = (-1)^{k+1}\hat{m}_{n,k}^{(\varphi)}(t)e^{ik(\varphi+\pi)}(-\boldsymbol{\varphi})$$
$$\equiv (-1)^{k+1}\hat{m}_{-n,k}^{(\varphi)}(t)e^{ik\varphi}\boldsymbol{\varphi},$$

$$\hat{m}_{n,k}^{(z)}(t)e^{ik\varphi}\mathbf{z} = (-1)^k\hat{m}_{n,k}^{(z)}(t)e^{ik(\varphi+\pi)}\mathbf{z}$$
$$\equiv (-1)^k\hat{m}_{-n,k}^{(z)}(t)e^{ik\varphi}\mathbf{z},$$
$$(B3)$$

where we have used $\boldsymbol{\rho} \to -\boldsymbol{\rho}$ and $\boldsymbol{\varphi} \to -\boldsymbol{\varphi}$ when $\varphi \to \varphi + \pi$. Therefore, $\hat{m}_{n,k}^{(\rho,\varphi)}(t)$ are even/odd functions of n as k is odd/even while $\hat{m}_{n,k}^{(z)}(t)$ is even/odd as k is even/odd. At $\rho = 0$, we take (see Ref. 27)

$$\hat{m}_{0,k}^{(\rho,\varphi)}(t) = 0, \quad |k| \neq 1,$$

$$\hat{m}_{0,k}^{(z)}(t) = 0, \quad k \neq 0,$$

$$\frac{\partial \hat{m}_{0,\pm 1}^{(\rho,\varphi)}}{\partial \rho}(t) = 0, \quad \frac{\partial \hat{m}_{0,0}^{(z)}}{\partial \rho}(t) = 0. \quad (B4)$$

The derivative conditions in Eq. (B4) are approximated by use of one-sided differences to obtain an estimate of $\hat{m}_{0,\pm 1}^{(\rho,\varphi)}(t)$ and $\hat{m}_{0,0}^{(z)}(t)$. The symmetries in Eq. (B3) and the conditions in Eq. (B4) enable the use of centered finite differences, even near the origin. An explicit, Runge-Kutta second-order time-stepping method is used to advance the discretized version of Eq. (1) forward in time while renormalizing the magnitude of $\mathbf{m}$ after every time step to preserve the constraint $|\mathbf{m}| = 1$. To avoid severe time-step restrictions due to the small grid spacing near the origin ($\approx 2\pi\rho_n/M$), we apply a smooth, radial grid dependent angular mask that effectively reduces the number of angular modes at ρ_n from M to $M_n = 2\pi/k_n$

$$g_n(k) = \frac{1}{2} + \frac{1}{2}\tanh\left(\frac{k_n - |k|}{\Delta k}\right).$$

The mask's parameters are the radial grid dependent wave number cutoffs k_n, $n = 1, \ldots, N$ and the cut-off width Δk. Application of the mask at every time step filters out numerically induced small wavelengths near the origin.[28] The cutoffs k_n are chosen so that the approximate grid spacing is $2\pi\rho_n/M_n \sim d\rho_{in}$, hence the grid near the origin has an effective spacing of $d\rho_{in}$. The mask applied to $\hat{m}_{n,k}^{(z)}(t)$ takes the form

$$\mathcal{G}^{(z)}\{\hat{m}^{(z)}(t)\}_{n,k} = g_n(k)\hat{m}_{n,k}^{(z)}(t).$$

Care must be taken when applying the mask to the in-plane Fourier coefficients $\hat{m}_{n,k}^{(\rho,\varphi)}(t)$ because $\boldsymbol{\rho}$ and $\boldsymbol{\varphi}$ depend on the grid location. We use

$$\mathcal{G}^{(\rho)}\{\hat{m}^{(\rho)}(t)\}_{n,k} = \frac{1}{2}\{[g_n(k-1) + g_n(k+1)]\hat{m}_{n,k}^{(\rho)}(t)$$
$$+ i[-g_n(k-1) + g_n(k+1)]\hat{m}_{n,k}^{(\varphi)}(t)\},$$

$$\mathcal{G}^{(\varphi)}\{\hat{m}^{(\varphi)}(t)\}_{n,k} = \frac{1}{2}\{i[g_n(k-1) - g_n(k+1)]\hat{m}_{n,k}^{(\rho)}(t)$$
$$+ [g_n(k-1) + g_n(k+1)]\hat{m}_{n,k}^{(\varphi)}(t)\}.$$

Numerical parameters we use are: $d\rho_{in} = 0.048\rho_*$, $d\rho_{out} = 0.25\rho_*$, $w = 10$, $\hat{n} = 126$, $M = 32-128$, $N = 222$, $L = 30\rho_*$, $k_1 = 4$, and $\Delta k = 1$. We find no significant change in the presented results for more accurate grids and filtering parameters.

In order to nucleate a droplet, we use initial conditions that are saturated in the **z** direction with a current that is above threshold. The small amplitude instability investigated in Sec. IV leads to the formation of a droplet. For the computation of the frequencies of the droplet in Fig. 7 found from micromagnetics, we take the Fourier transform of the spatially averaged magnetization time series from the simulation and extract the frequency with the largest power. The frequency resolution is finer than the size of the dots in Fig. 7.

---

*mahoefer@ncsu.edu

[1] N. N. Akhmediev and A. Ankiewicz, Lect. Notes Phys. **751**, 1 (2008).

[2] B. A. Ivanov and A. M. Kosevich, Zh. Eksp. Teor. Fiz. **72**, 2000 (1977).

[3] A. M. Kosevich, B. A. Ivanov, and A. S. Kovalev, Phys. Rep. **194**, 117 (1990).

[4] M. J. Ablowitz and H. Segur, *Solitons and the Inverse Scattering Transform* (SIAM, Philadelphia, 1981).

[5] A. K. Zvezdin and A. F. Popkov, Sov. Phys. JETP **57**, 350355 (1983); B. A. Kalinikos, N. G. Kovshikov, and A. N. Slavin, JETP Lett. **38**, 413 (1983); P. DeGasperis, R. Marcelli, and G. Miccoli, Phys. Rev. Lett. **59**, 481 (1987); B. A. Kalinikos, N. G. Kovshikov, and A. N. Slavin, Phys. Rev. B **42**, 8658 (1990); M. Chen, M. A. Tsankov, J. M. Nash, and C. E. Patton, Phys. Rev. Lett. **70**, 1707 (1993).

[6] J. C. Slonczewski, J. Magn. Magn. Mater. **159**, L1 (1996).

[7] L. Berger, Phys. Rev. B **54**, 9353 (1996).

[8] J. C. Slonczewski, J. Magn. Magn. Mater. **195**, 261 (1999).

[9] E. B. Myers, D. C. Ralph, J. A. Katine, R. N. Louie, and R. A. Buhrman, Science **285**, 867 (1999); J. A. Katine, F. J. Albert, R. A. Buhrman, E. B. Myers, and D. C. Ralph, Phys. Rev. Lett. **84**, 3149 (2000).

[10] S. I. Kiselev, J. C. Sankey, I. N. Krivotorov, N. C. Emley, R. J. Schoelkopf, R. A. Buhrman, and D. C. Ralph, Nature (London) **425**, 380 (2003); W. H. Rippard, M. R. Pufall, S. Kaka, S. E. Russek, and T. J. Silva, Phys. Rev. Lett. **92**, 027201 (2004).

[11] D. Ralph and M. Stiles, J. Magn. Magn. Mater. **320**, 1190 (2008).

[12] T. Silva and W. Rippard, J. Magn. Magn. Mater. **320**, 1260 (2008); J. A. Katine and E. E. Fullerton, *ibid.* **320**, 1217 (2008).

[13] A. Slavin and V. Tiberkevich, Phys. Rev. Lett. **95**, 237201

(2005).

[14] N. L. Schryer and L. R. Walker, J. Appl. Phys. **45**, 5406 (1974); J.-Y. Lee, K.-S. Lee, S. Choi, K. Y. Guslienko, and S.-K. Kim, Phys. Rev. B **76**, 184408 (2007).

[15] J. Nielsen, IEEE Trans. Magn. **12**, 327 (1976); E. A. Giess, Science **208**, 938 (1980).

[16] K. Y. Guslienko, W. Scholz, R. W. Chantrell, and V. Novosad, Phys. Rev. B **71**, 144407 (2005); V. Novosad, F. Y. Fradin, P. E. Roy, K. S. Buchanan, K. Y. Guslienko, and S. D. Bader, *ibid.* **72**, 024455 (2005).

[17] G. Gioia and R. D. James, Proc. R. Soc. London, Ser. A **453**, 213 (1997).

[18] M. A. Hoefer, T. J. Silva, and M. D. Stiles, Phys. Rev. B **77**, 144401 (2008).

[19] J. Kevorkian and J. D. Cole, *Multiple Scale and Singular Perturbation Methods* (Springer, New York, 1996).

[20] D. V. Berkov and N. L. Gorn, Phys. Rev. B **76**, 144414 (2007).

[21] B. Piette and W. J. Zakrzewski, Physica D **119**, 314 (1998).

[22] Ya. B. Bazaliy, B. A. Jones, and S.-C. Zhang, Phys. Rev. B **69**, 094421 (2004); S. Mangin, D. Ravelosona, J. A. Katine, M. J. Carey, B. D. Terris, and E. E. Fullerton, Nature Mater. **5**, 210 (2006); C. Serpico, G. Bertotti, R. Bonin, M. d'Aquino, and I. D. Mayergoyz, J. Appl. Phys. **101**, 09A507 (2007).

[23] M. A. Hoefer, M. J. Ablowitz, B. Ilan, M. R. Pufall, and T. J. Silva, Phys. Rev. Lett. **95**, 267206 (2005).

[24] M. D. Stiles, J. Xiao, and A. Zangwill, Phys. Rev. B **69**, 054408 (2004).

[25] N. R. Cooper, Phys. Rev. Lett. **80**, 4554 (1998).

[26] S. Komineas and N. Papanicolaou, Physica D **99**, 81 (1996).

[27] A. Iserles, *A First Course in the Numerical Analysis of Differential Equations* (Cambridge University Press, Cambridge, 2008).

[28] B. Fornberg, SIAM J. Sci. Comput. **16**, 1071 (1995).